DISTRIBUTION OF MASS IN RELAXED FROG SKELETAL MUSCLE AND ITS REDISTRIBUTION UPON ACTIVATION

L. C. Yu,* A. C. Steven,* G. R. S. Naylor,* R. C. Gamble,‡ and R. J. Podolsky*
*Laboratory of Physical Biology, National Institute of Arthritis, Diabetes and Digestive and Kidney Diseases, National Institutes of Health, Bethesda, Maryland 20205; and ‡Division of Chemistry and Chemical Engineering, California Institute of Technology, Pasadena, California 91125

ABSTRACT Five orders of equatorial reflection were recorded from both relaxed and fully activated intact frog sartorius muscle using synchrotron x-ray radiation. Electron density maps of the myofilament lattice in axial projection were calculated from the integrated intensities by Fourier synthesis, using all possible phase combinations. These maps were evaluated systematically in terms of their compatibility with electron microscopically and biochemically derived properties of the lattice structure and with the minimum wavelength principle. For the relaxed state, one phase combination emerged as most consistent with these constraints: it shows a thick filament with a compact core surrounded by an annular shell of density. The distribution of mass suggests that (a) the S-2 moiety of the myosin molecule is an integral part of the thick-filament backbone and (b) the S-1 moiety makes up the shell and is tilted or slewed around the backbone. For the active state, there are two feasible maps, which differ according to whether or not the activation process is associated with phase inversion in two of the reflections. Both maps represent patterns of redistribution of mass upon activation in which the thick-filament backbone is practically unaffected and there is movement of density from the annular shell towards the thin filaments. In addition to this outward radial flux of density from the thick-filament periphery, the pattern of net mass transfer involves a pronounced azimuthal component in both cases. The total net mass transfer is equivalent to ~20% (no phase change) or ~40% (with phase change) of the S-1 mass. From the observed systematic increase in peak widths of the higher orders, the size of the crystalline domain in the myofilament lattice in the relaxed sartorius is estimated to be >650 nm and the variations in myofilament lattice spacing among different myofibrils to be about ±3%. Furthermore, in the activated state, the equilibrium positions of the myofilaments are no longer well ordered, but are distributed statistically about the lattice points with a standard deviation of ~3 nm.

INTRODUCTION

Although the central role of actomyosin cross-bridges in muscle contraction is widely accepted, neither the distribution of mass within the myofilament array in relaxed muscle cells nor the molecular movement associated with crossbridge formation is known in detail. Information regarding these points, which is essential for a full understanding of the cross-bridge mechanism, has been derived primarily from the equatorial x-ray diffraction patterns of muscle cells in various physiological states (1–5). Changes in the intensities of the two strong inner reflections *10* and *11* accompany changes in the physiological state. For instance, *10* becomes weaker and *11* becomes stronger upon activation, and further changes occur when the muscle goes into rigor. To explain these changes Huxley (1), and later Haselgrove and Huxley (2), suggested that mass is shifted from the thick-filament region to the thin-filament region in transitions from the relaxed state to either the fully activated or the rigor state.

Evidence is strong that the mass transfer inferred from x-ray diffraction patterns is directly related to cross-bridge formation between the thick and thin filaments. An apparent increase in diameter of thin filaments at the expense of the thick filaments on transition from the relaxed to the rigor state was inferred from electron microscopy (1). Later, it was shown that graded levels of isometric force are accompanied by an almost linear change in the intensity ratio I_{11}/I_{10} (5).

Hitherto, most studies have been based on the two reflections *10* and *11*, and so spatial resolution was limited to ~20 nm. At this resolution, the two-dimensional density maps show both sets of projected filaments as undifferentiated, cylindrically symmetrical concentrations of mass without visible substructure (Fig. 6). Higher-order reflections as far as *30* at $(12 \text{ nm})^{-1}$ have been observed in the relaxed state (6–8), but no higher-order pattern has yet been reported for the active state. Accordingly, the nature of the mass movement at this level of detail is not known. In

the present study, we obtained the intensity of three higher orders, *20, 21, 30,* from frog sartorius muscle in the fully activated state as well as the relaxed state by using the intense x-ray source at Stanford Synchrotron Radiation Laboratory (SSRL).[1] Using these data we synthesized electron density maps corresponding to all possible phase combinations, and evaluated them systematically in terms of available information on the myofilament lattice structure. This analysis led to a single model for the relaxed state and two possible models for the active state. Comparison of the density maps for the relaxed and active states has revealed several new aspects of the pattern of redistribution of mass upon activation.

METHODS

X-ray Diffraction

To obtain sufficient scattering from the brief periods during which muscle can be fully activated without significant decrease in developed force, the intense x-ray flux produced by synchrotron radiation from the electron-positron storage ring at Stanford Linear Accelerator Center was used. The x-ray beam at Experimental Station I-4 of SSRL was focused and monochromatized by a combination of a 125-cm mirror and a 7-cm monochromator (9). The wavelength selected by the monochromator for this set of experiments was 0.171 nm and the resultant photon intensity at the focal point was estimated by means of an ionization chamber to be ~6 × 10^9 photons/s at 3.1 GeV and 60 mA. The beam, measured by a photodiode array (10), was 1 mm high and 2 mm wide at the specimen and 300 μm high and 4 mm wide at the focus. The distance between specimen and detector was 1 m.

X-ray data were recorded by a position-sensitive detector (11). Because the carbon-coated quartz wire in the detector (25 μm diam) could be damaged by an excessive flux of incident photons, nickel foils (generally

---

[1] The following abbreviations are used in this paper: Stanford Synchrotron Radiation Laboratory, SSRL; myosin subfragment 1, S-1; myosin subfragment 2, S-2; and light meromyosin, LMM.

50 μm thick) were placed before the second set of the guard slits immediately in front of the specimen holder whenever the count rate exceeded 15,000 counts/s.

The intensities of reflection peaks were found using a nonlinear least-squares fitting procedure (12) that took into consideration the systematic broadening of peak widths with increasing values of scattering angle (see Appendix). Fourier amplitudes were calculated from the intensities using the Lorentzian correction for fiber equatorial patterns, $F_{hk}^2 \propto I_{hk}(h^2 + k^2 + hk)^{1/2}$.

Physiological Procedures

Sartorius muscles dissected from *Rana pipiens* frogs (Rand-McNally, Somerset, WI) were stimulated every 2 min for 2–3 h at 20–22°C. At the end of each experiment, the force level generally had dropped by <20% of the initial value. For the four experiments reported here, the initial relaxed sarcomere length determined by laser diffraction was 2.2–2.25 μm and the final length measured after the experiment was 2.15–2.2 μm; typically the sarcomere length decreased ~0.1 μm during activation. For each stimulation cycle, data for the relaxed pattern was accumulated for 1 s just before the onset of stimuli. Data for the active pattern were recorded for 0.2 s after the force reached maximal level. Total accumulated exposure time for the active pattern was 20–30 s.

Fourier Syntheses

Fourier syntheses were performed by combining the experimental amplitudes with chosen sets of phases, and then obtaining the corresponding density maps by inverse Fourier transformation. These operations were performed and the resulting maps displayed using the PIC system (13) on a PDP 11/70 computer (Digital Equipment Corp., Marlboro, MA). The myofilament lattice was represented on an approximately hexagonal point lattice (14) with 36 samples per lattice repeat, giving a sampling rate of (1.05 nm)$^{-1}$. The Fourier amplitudes were taken to be equal for diffraction from all sets of lattice planes with the same spacings (e.g., $F_{10} = F_{01} = F_{1\bar{1}}$ for the three contributions to the first equatorial peak). This assumption requires in effect that the projected structure observes threefold rotational symmetry, which is justified since the thick filament is three stranded (15–18). As in earlier studies of this type (e.g., 4, 20), the projected unit cell was assumed to be centrosymmetric, and thus the phases were taken to be 0 or π. In fact, an individual thick filament has a ninefold symmetry in axial projection (15), which is not centrosymmetric.
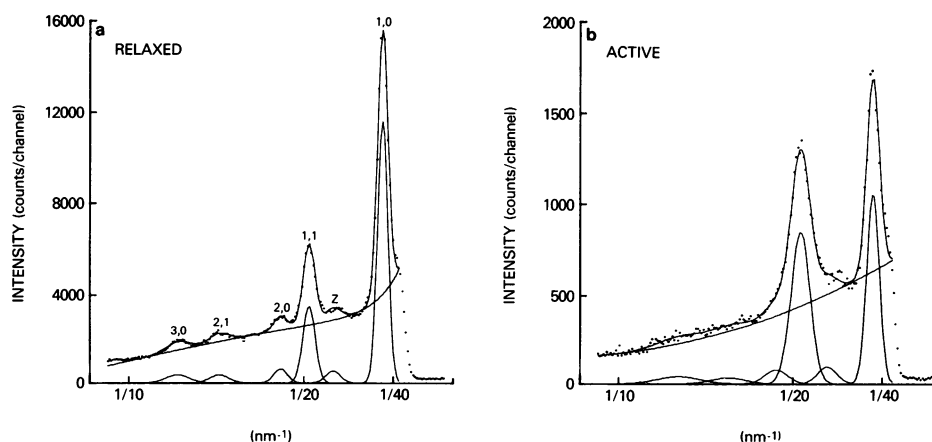
FIGURE 1 Equatorial diffraction pattern of frog sartorius in (*a*) relaxed state and (*b*) fully activated isometric contraction at 20–22°C. Force level following the series of activation cycles remained within 15% of its initial value. The composition of the Ringer's solution was (in millimoles per liter): NaCl, 115; KCl, 2.5; CaCl$_2$, 1.8; Na$_2$HPO$_4$, 3.1 (pH 7.0). Detector to specimen distance was 1 m. Total exposure time in *a* was 200 s; in *b* 25 s. Average count rate was 12,000/s. Dots are original data; solid lines obtained by a least-squares fitting procedure. In *a* the intensity above background at ~1/10 nm^{-1} is probably due to the reflection doublet *22* and *31*; these reflections were not analyzed because they were too close to the edge of the detector.

However, since no reflections originating from the superlattice (19) have been observed on the equator with the frog muscle, the thick-filament contribution to the equatorial pattern is an average of two filaments, separated by azimuthal rotation of 180°. This would give the average filament visualized 18-fold symmetry. In consideration of the fourth order 21, it was further assumed that $F_{12} = F_{21}$. If this were not the case, a skewness would be introduced into the axial projection map which, at the present resolution, would not be compatible with the high order of rotational symmetry.

Care was taken to make the x-ray beam sample the same portion of the muscle in the relaxed and active states. Thus the zero-order Fourier component, F_{00}, which is proportional to the total amount of mass in the beam, stayed essentially the same and the data sets were standardized by assigning the value of 1,000 (arbitrary units) to this amplitude. Normalization was completed by setting the amplitude F_{10}(relaxed) to be 100.

Difference Maps

To visualize mass transfer on transition from the relaxed to the active state, difference maps between the respective density distributions were constructed and displayed. With the normalization conventions described above, such maps represent the net redistribution of projected mass within the unit cell of the myofilament lattice. To facilitate interpretation of these images, color coding was used to distinguish those locations that incur net gains from those that incur net losses and those that are effectively unchanged.

Computational Model-Building Experiments

The PIC system of programs and its associated image processing hardware (13) were used in numerical modeling experiments for several purposes (see Results):

(a) To test the consistency of structural features of a given phase model with respect to the variations encountered between the amplitudes from different experiments;

(b) to estimate the apparent diameters of the filaments at our working resolution, the thick-filament backbone and the thin filament were modeled as cylindrically symmetric structures with bell-shaped density contours (with Gaussian profiles) having outer diameters of 15 and 7.5 nm, respectively (17, 18, 20, 21), situated at the appropriate lattice sites. When restricted to a spatial resolution of 12 nm, (by band-limiting in reciprocal space) the densities fell to zero at effective diameters of 19 and 15 nm[1], respectively, and these limits were used in the mass integrations for the various phase models;

(c) to investigate the smearing effect of the relatively low resolution by constructing models of defined features in real space, obtaining their Fourier transforms and band-limiting them. After inverse Fourier transformation, such resolution-limited images may then be compared quantitatively with the originals;

(d) to integrate the cumulative amounts of visible mass (i.e., above background) associated with the thin-filament sites and the myosin filament backbone in each of the phase models.

Estimation of Invisible Mass

A calculation was also made to assess the maximum extent to which interfilament protein could affect the amount of filament protein visible above background. For a fixed amount of total protein, the spatial distribution that gives the greatest amount of "invisible" (i.e., back-

---

[1]Recently, it has been proposed that the outer diameter of the thin filament is 10 nm (34). We have repeated these calculations using this value, and find the resulting mass ratios (see Results) to be quite unaffected by this change. The reason for this is that at 12-nm resolution there is no significant difference between the respective effective diameters of a 7.5-nm and a 10.0-nm thin filament.

ground) mass is the one with the highest value of minimum density: in the myofilament lattice, this corresponds to a uniform average density in the interfilament spaces. To construct this limiting model distribution, we allocated the appropriate amounts of mass for the actin filament and for the myosin filament backbone (either including the S-2 moiety, or not) to cylinders of uniform density, with diameters of 7.5 and 15 nm, respectively. The remaining protein, myosin S-1 (with or without S-2) together with other soluble protein believed to amount to no more than one-third of the total filament protein (22, 23), must occupy the remainder of the unit cell. The masses used are given in the section Phase Selection for the Relaxed State. In this extreme case, 76% of total mass is "invisible" when the S-2 is taken to be totally without the myosin filament backbone, or 64%, with the S-2 entirely included within the backbone. These limits are not influenced by the limited-resolution effect because the minimum density value initially applies to such a large fraction of the total unit-cell area that this value is not increased upon band-limiting. These numbers were used to calculate how the myosin/actin ratios derived from the distributions of visible mass for each of the phase models (Table II) are affected by the maximum feasible amount of underlying "invisible" mass.

RESULTS

Integrated Intensities of Equatorial Reflections

Fig. 1 shows typical reflection patterns obtained from the same sartorius in relaxed and fully activated states. Compared with the two strong reflections, the three higher orders of the resting pattern are relatively weak but clearly defined. For the activated state the corresponding peaks are much broader, with the higher-order peaks partially merging into each other.

In all, 12 experiments were performed. From those, data were selected for analysis according to the following criteria: (a) at the end of the experiment, the force level of the muscle should have retained at least 80% of its initial value; (b) the lattice spacing d_{10} for the active and the relaxed patterns should differ by $<4\%$; (c) the laser pattern should have remained clear in tetanus during the initial setup period and also at the end of the experiment. 4 out of 12 experiments met these criteria. Their patterns yielded the sets of reflection intensities listed in Table I. Upon activation, the normalized intensities of 20 increased slightly (by no more than 20%), whereas 21 and 30 decreased by $\sim 40\%$.

TABLE I
AVERAGE REFLECTION INTENSITIES
NORMALIZED WITH RESPECT TO TRANSMITTED
BEAM INTENSITY*

State	I_{10}	I_{11}	I_{20}	I_{21}	I_{30}
Relaxed	0.71	0.27	0.04	0.05	0.05
SEM‡	(0.05)	(0.03)	(0.004)	(0.01)	(0.01)
Active	0.42	0.60	0.05	0.03	0.03
SEM	(0.03)	(0.08)	(0.01)	(0.01)	(0.01)

*Individual intensities from four experiments: first normalized by the transmitted beam, then averaged.
‡Standard error of the mean.

Fourier Syntheses

There are eight choices for the phases of the five reflections after _10_ and _11_ are assigned phases of 0°. Among the electron density maps to which these phase sets correspond, further eliminations were made as follows.

Phase Selection for the Relaxed State. The mass of the thick-filament backbone relative to that of the two thin filaments in a unit cell was used as the first criterion. Masses within the apparent diameters of the filaments (see Methods) were determined by integration for each density map (Table II). From known biochemical

TABLE II
CALCULATED MASSES (IN ARBITRARY UNITS) OF THICK FILAMENT BACKBONE AND THIN FILAMENTS IN THE MYOFILAMENT UNIT CELL‡

Model§	Total visible mass‖	MY19*¶	ACT15*¶	Other	$\frac{MY19*}{ACT15*}$‡‡
			Relaxed state		
A_r	534	196	128	210	1.53
B_r	781	230	167	384	1.38
C_r	597	221	137	239	1.61
D_r	566	212	117	237	1.81
			Active state		
A_a	595	201	177	217	1.14
B_a	778	226	205	347	1.10
C_a	639	219	183	237	1.20
D_a	512	198	142	172	1.38

Mass shift, Δ§§

From model $B_r \rightarrow$ model B_a, Δ = 47; from model $B_r \rightarrow$ model D_a, Δ = 118

‡Model calculations based on 12-nm resolutions and the diameter of thick-filament backbone and thin filament being 15 and 7.5 nm, respectively.
§Phase combinations for models A, B, C, D are as shown in Fig. 2.
‖Total visible mass = total mass of the unit cell above the minimum density level = 1,000 − minimum density × 44 × 72; unit cell dimensions are 44 × 72.
¶MY19* = total mass calculated above the minimum (background) level within the apparent diameter 19 nm at the lattice point of the unit cell; ACT15* = total mass above the minimum level within the apparent diameter 15 nm at the two trigonal points of the unit cell.
‡‡The ratio given in the table is between the corresponding amounts of visible mass. The ratio of the mass of the thick-filament backbone to that of the thin filament expected from biochemical data is 1.28 or 0.76, according to whether S-2 is part of, or external to, the backbone (see footnote 2). When extreme limits for the amounts of invisible mass are estimated in these two cases (see Methods), the ratios for the relaxed states become 1.01–1.16 (S-2 in backbone) or 0.94–1.03 (S-2 external to backbone).
§§Mass shift = $1/2 \int_{unit \, cell} |\rho_{X_a} - \rho_{Y_r}| dA$, where ρ_{X_a} and ρ_{Y_r} are density distributions of models X_a and Y_r, respectively. With the normalization conventions used, these integrals are independent of the amounts of invisible mass present in models X_a and Y_r.

data we calculate the mass ratio of light meromysin (LMM) to two thin filaments in a sarcomere of 2.2 μm to be 0.76. If one includes the entire myosin rod (i.e., LMM + S-2) within the thick-filament backbone, this mass ratio increases to 1.28.[2] In consideration of experimental errors, we conservatively rejected those models that gave a value of >2 for this ratio. After imposing this criterion, five models remained.

One phase combination (+ + - + -) was rejected because it did not satisfy the minimum wavelength principle (24), which imposes a constraint on the number of phase changes that can take place within the spacing $2d^{-1}$ in the Fourier transform of any object of maximal dimension d (here d_{10}).

The remaining four models for the relaxed state (A_r, B_r, C_r, and D_r) are shown in Fig. 2. Model C_r (+ + ---) (Fig. 2 C) has a pronounced low density core (~10 nm diam) at the center of the thick-filament backbone. To observe such a "hole" at 12-nm resolution, the minimum possible diameter of a totally empty hole is 5 nm, as determined by computational model-building experiments. In the absence of any evidence for a low density core on this scale running the entire thick-filament length in frog muscle, model C_r was discarded.

Model A_r (+ + - - +) (Fig. 2 A) was first proposed by Haselgrove et al. (4) based on data obtained in this laboratory (3, 8). However, we consider this model to be unlikely because its thick filament shows a sharply defined sixfold symmetry immediately surrounding the backbone, which is at odds with the expected 18-fold symmetry for the three-stranded myosin filament in frog sartorius (20 [p. 592], 15, 19).

Model D_r (+ + + - +) (Fig. 2 D and 3 b) also shows sixfold structure surrounding the thick filament. Here the sixfoldedness takes the form of a substantial amount of mass protruding from the thick filaments towards the spaces between the thin filaments. Such an effect could take place if there were direct interaction between the myosin heads and the thin filaments, but at present there is no evidence for such interaction at physiological ionic strength. Moreover, the mass ratio of MY19*/ACT15* (Table II) is 1.8, which indicates that with this phase combination the mass is overly concentrated in the thick-filament shaft. Thus we consider that this model is also unlikely.

Model B_r (+ + - + +) (Figs. 2 B and 3 a) satisfies all

[2]The MY/ACT mass ratios were calculated largely from data compiled by Squire (14). To estimate the backbone mass of a thick half filament, two cases were considered according to whether the backbone consisted of the LMM or the rod moieties, together with the C-protein molecules. These alternatives gave a total mass of 2.32 × 10⁷ or 3.89 × 10⁷ daltons, respectively. The unit cell thin-filament mass calculated for a sarcomere length of 2.2 μm is 3.04 × 10⁷ daltons. Therefore MY/ACT = 0.76 or 1.28, depending on whether the backbone of the thick filament contains the LMM or the rod moieties of the myosin molecule. The total S-1 and associated light chains contain 38% of the unit cell mass.
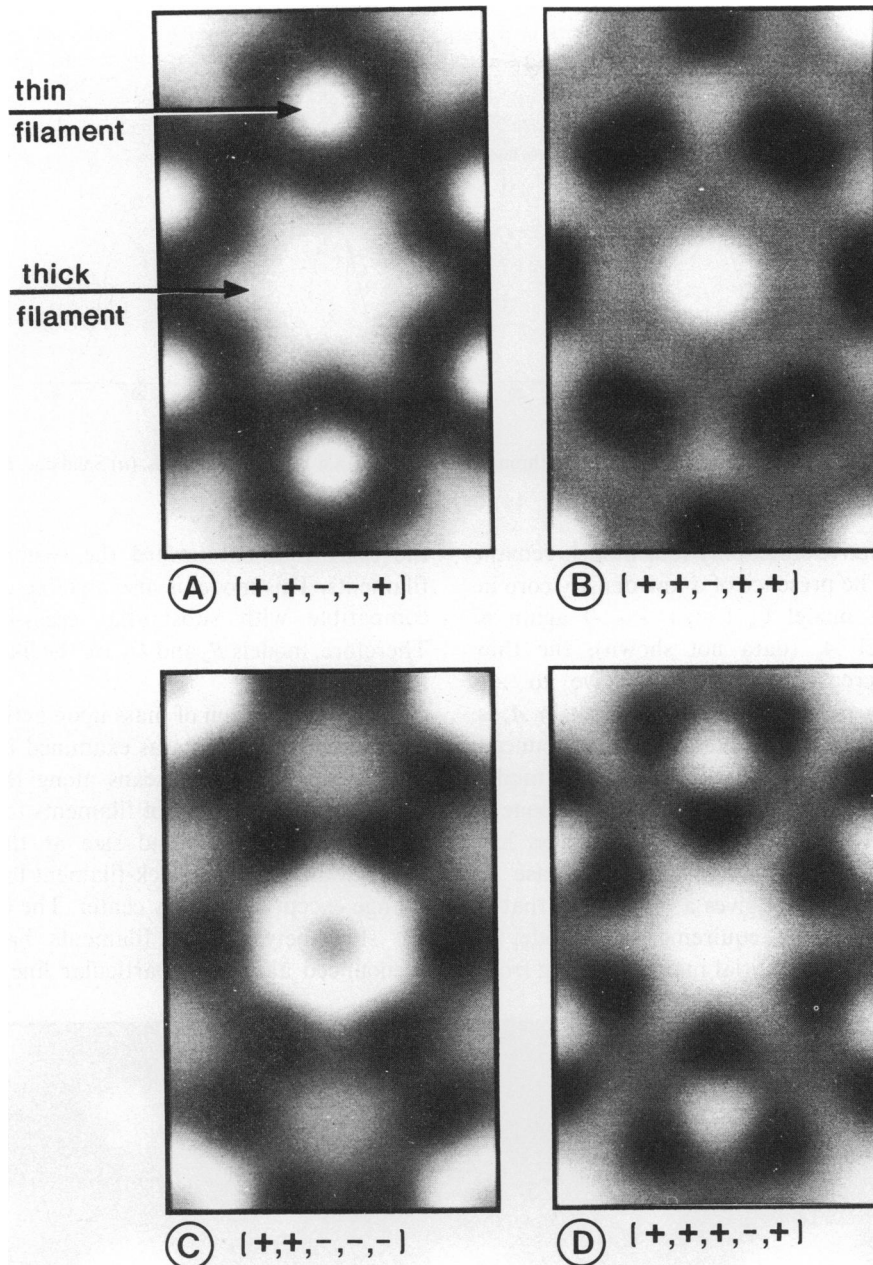
FIGURE 2 Electron density maps of the myofilament lattice in axial projection for relaxed frog sartorius muscle. All four maps (*A–D*) were constructed by Fourier synthesis using the same set of amplitudes. The myofilament lattice was represented on an approximately hexagonal point lattice (14) with 36 samples per lattice repeat. All four maps are represented according to a standard gray scale in which the regions of highest density are represented in the lightest tones. The maps have been normalized so that their respective unit cells contain the same total mass. The center-to-center spacing between thick filaments is 44 nm.

the requirements. Its mass ratio of MY19*/ACT15* is 1.4, and the shell of density surrounding the backbone shaft is consistent with the expected high order of azimuthal symmetry. We conclude that model B_r most likely represents the distribution of mass in relaxed sartorius.

To present the density distribution of B_r in more detail, Fig. 3 (solid line) shows a scan along the line passing through the centers of the thick and thin filaments. The mass distribution is consistent with a thick-filament backbone of 15 nm diam and a thin filament of 7.5 nm diam. In

addition, there is a substantial amount of mass in the interfilament space. This annular shell of mass occupies the region between 11 and 15 nm in radius from the center of the filament.

Phase Selection for the Active States. In principle, the same 32 phase sets may apply to the amplitudes measured for the active state. However, after imposing the minimum wavelength principle and the restriction that the mass ratio of MY19*/ACT15* (Table
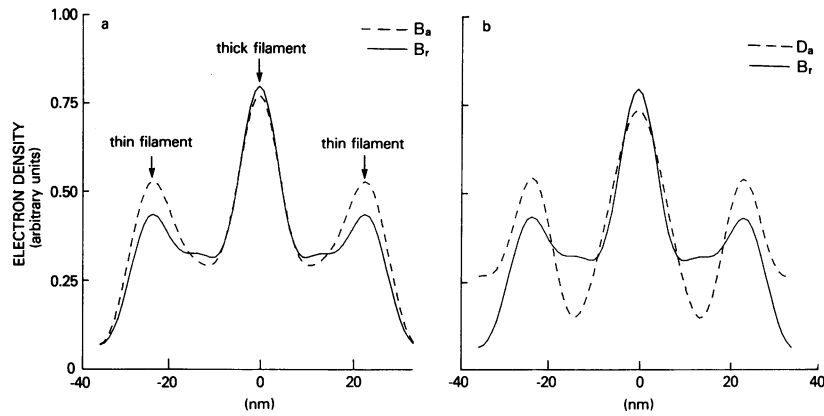
FIGURE 3   Electron density scanned along the line passing through the centers of thin and thick filaments. (*a*) Solid line, B_r state; dashed line, B_a state. (*b*) Solid line, same as in (*a*); dashed line, D_a state.

II) also be <2 in the active state, only four models remain (A_a, B_a, C_a, and D_a). The presence of a low-density core in the thick filament of model C_a (+ + - - -) again is implausible. In model A_a (data not shown), the thin filament has an increased diameter relative to A_r. Although the sixfold aspect of the thick filament in A_a is not as sharply defined as in A_r, it is still a pronounced feature of this model and discriminates against it. In model B_a (Figs. 3 *a* and 4), the shell surrounding the backbone is much less dense than in B_r, and substantial mass has accumulated at the trigonal points. As in the case of relaxed muscle, the *B* phase set gives a model (B_a) that is compatible with the symmetry requirements. In model D_a (Figs. 3 *b* and 4), we find interstitial mass extending from

the thick filament toward the region between the thin filaments. This model is also a viable candidate, since it is compatible with substantial cross-bridge attachment. Therefore, models B_a and D_a are the likeliest candidates for the active state.

The redistribution of mass upon activation by transition from B_r to B_a or to D_a was examined in detail. In Fig. 3 *a* are shown the density scans along the lines joining the centers of the two types of filaments for models B_r and B_a. The gain in density and size at the thin filament is substantial, while the thick-filament backbone shows little change except at the very center. The change of density of the shell between the filaments happens to be least pronounced along this particular line. Loss is greater in
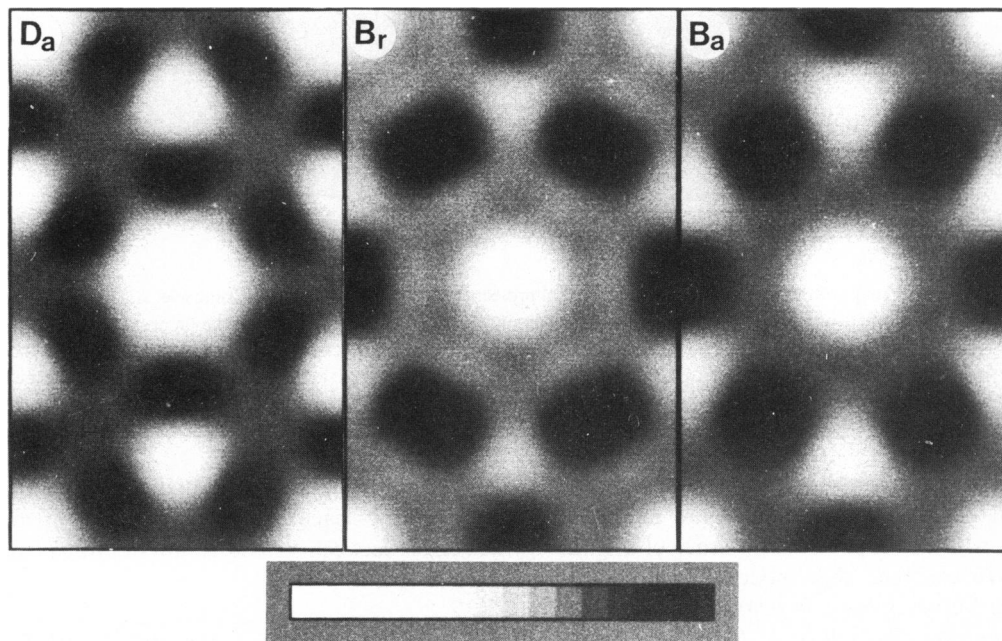

FIGURE 4   Electron density maps of the myofilament lattice of frog sartorius muscle showing the redistribution of density that accompanies activation. B_a and D_a represent the two possible configurations for the active state; B_r shows the relaxed muscle, for comparison. All three maps are depicted according to the same grayscale (see ramp at bottom).

other parts of the unit cell (see below). Fig. 3 b shows the transition from B_r to D_a. Here, the redistribution of mass is substantially greater than in Fig. 3 a.

The color-coded difference maps (Fig. 5) provide an overall view of the mass movement in two dimensions. Several features are common to both difference maps and therefore are taken as properties of the activation process.

(a) The mass within the backbone of apparent diameter 19 nm remains essentially unchanged upon activation, particularly if the transition is from B_r to B_a. The gray-tone region around the thick-filament lattice point in the difference map of B_a-B_r, which represents areas of relatively unchanged density, is 19 nm across. The total mass inside this area changes by only 1% (Table II). For the difference map (D_a-B_r), the corresponding gray-tone area is 21 nm across and the total mass change is 6% (Table II).

(b) The distribution of mass shift away from the thick-filament backbone is significantly nonuniform.

(c) Net density loss is mostly shifted from the region peripheral to the thick-filament backbone and is gained by the region surrounding or at the trigonal points.

The total amount of net mass movement depends on whether there is a phase change upon activation (Table II). If the transition is from B_r to B_a, then the net mass shift visualized is equivalent to 6% of the total mass above the background level in B_r, whereas if the transition is from B_r to D_a, the corresponding amount is 15%.

DISCUSSION

The major results in the present study are (a) measurement of the equatorial reflection intensities as far as 30 for actively contracting muscle, and (b) assignment of phases to these reflections for both relaxed and activated muscle. By imposing known myofilament properties as quantitative constraints, an electron density map for the relaxed myofilament lattice in axial projection is derived. Similarly, two such maps are admissible for the active state. Our relaxed map (model B_r in Fig. 2) is based upon different phases from the model previously proposed by others (4) (model A_r in Fig. 2). It reveals new structural features, particularly in regard to the distribution of myosin heads around the thick-filament backbone. The two candidates for the active state differ from each other in some details (Fig.4) but share certain essential features. Both yield difference maps whose common features reveal new aspects of the configurational change that takes place within the myofilament lattice upon activation.

The present study represents an approximately twofold improvement in resolution over structural studies in which only 10 and 11 were used (2, 5). Fig. 6 shows how myofilament substructure is progressively differentiated by including additional reflections in the Fourier synthesis. The thick filament is resolved into a backbone with mass distributed around it only when five reflections are used.
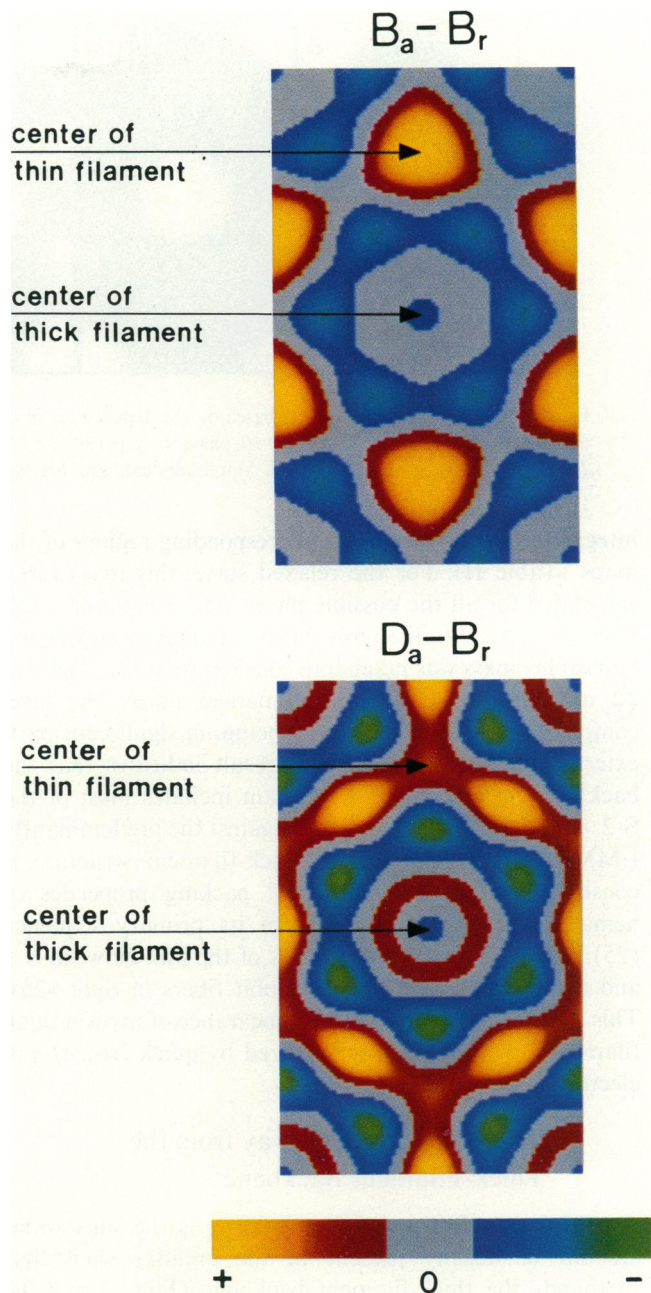

FIGURE 5 Color-coded difference maps that illustrate patterns of redistribution of mass upon activation from the relaxed state. These two maps represent two different possibilities for the active state, from which the map (B_r) of the relaxed muscle has been subtracted. Strong gains in density are shown as yellow, and lesser but nevertheless significant positive changes are shown as red. Similarly, moderate and strong losses are represented as blue and green, respectively. Regions in which no significant change has taken place (quantitatively, <20% of the maximum recorded) are mapped in gray.

S-2 Probably Forms an Integral Part of the Thick-Filament Backbone

The relative masses associated with the thin filaments and with the thick-filament backbone were calculated by
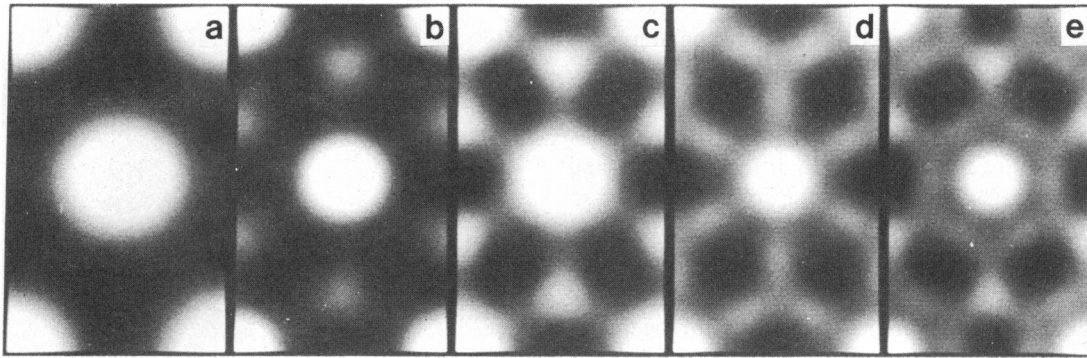
FIGURE 6   Electron density maps based on the deduced set of phases, showing the additional detail obtained by including an increasing number of reflections. (a) Reflection: 10, phase: (+); (b) 10 and 11, (+ +); (c) 10, 11, and 20, (+ + -); (d) 10, 11, 20, and 21, (+ + - +); (e) 10, 11, 20, 21, and 30, (+ + - + +). Amplitudes used are those shown in Table I for the relaxed state.

integrating the density in the corresponding regions of the maps (Table II). For the relaxed state, this mass ratio, calculated for all the possible phase sets, was never <1.4. Even when an extreme limit for the amount of underlying "invisible" mass was taken into consideration (see footnote ‡‡ in Table II), this ratio remained above the level compatible with the S-2 moiety being, in significant part, external to the backbone. This result indicates that the backbone mass within 15 nm diam includes most of the S-2, which probably is retracted against the predominantly LMM shaft. This aspect of thick-filament structure is consistent with the hypothetical packing properties of nematode myosin, deduced from its primary sequence (25), and with inferred properties of the link between S-1 and the myosin backbone for rabbit fibers in rigor (26). This is also consistent with the appearance of myosin thick filaments (insect muscle) visualized by quick freeze/etch electron microscopy (27).

S-1 Heads Extend Away from the Thick-Filament Backbone

A conspicuous feature of the model B_r is the substantial amount of density present in the annular shell that surrounds the thick-filament backbone (Figs. 2 and 3). This distinguishes it from model A_r (4), where density in the region between the thick-filament backbone and the thin filament is more closely associated with the former. This shell extends to a radial limit of ~15 nm. A similar estimate of the outer diameter of the myosin filament has been made in a recent electron microscopic study (17).

The shell density peaks at r ~13 nm, and it is reasonable to interpret it as being contributed by the myosin S-1 moieties. As the annulus is resolved from the thick-filament backbone and does not appear coalesced with it, it seems probable that a substantial proportion of the S-1 moieties are offset from the outer wall of the backbone (and connected to it with a low density link). Because the shape of S-1 is approximately ellipsoidal, with the major axis 12 nm in length (28), and yet these molecules are inferred to

contribute the relatively thin (8 nm) annulus visualized here, it follows that the S-1 heads must either be oriented with their long axes at a relatively acute angle to the filament axis or slewed around the backbone (29).

Thick-Filament Backbone during Activation

In both difference maps, mass is shifted primarily from the region peripheral to the backbone, which itself remains almost unchanged. The overall constancy of the backbone density in both cases indicates that no radical relocation of the S-2 portion of LMM is associated with force generation. However, if S-1 attachment to actin were to result in a small displacement of myosin S-2 moieties away from the backbone of the thick filament (30), this would not be detected at the present resolution.

Outward Movement of Density from the Thick-Filament Periphery upon Activation

A significant feature of the difference maps is that both indicate a pronounced azimuthal component to the mass shift (Fig. 5). To transfer mass from the region of most pronounced loss (green) to that of prominent gain (yellow), a net rotation must occur. Despite the limited resolution (see below) and the fact that sixfold symmetry has been explicitly imposed upon these unit-cell maps, we consider that the observed nonuniformity is so marked that it represents a genuine effect, related to the sixfold distribution of the actin filaments around any given myosin filament. This indicates that upon activation, a substantial fraction of the myosin heads must rotate away from their equilibrium positions in the relaxed state to attach to the thin filaments, and that some must rotate by larger angles than others.

There has been discussion of whether the mass movement upon activation is primarily azimuthal (3) or radial (4). From the present study, it appears that both effects are

substantial, and that the net azimuthal component is indeed rather pronounced.

Net Amount of Mass Shift

With the B_r to B_a transition, the total amount of visible mass is effectively unchanged, and the net mass transfer amounts to 6% of it (Table II). Since the mass shift originates mostly from outside the thick-filament backbone, this figure represents ~20% of S-1 mass (as visualized in the annular shell). If the transition is $B_r \rightarrow D_a$ the net mass transfer is equivalent to 40% of the S-1 mass. With S-1 resolved from the backbone, the amount of net transfer is now attributable mostly to S-1 alone. It should be emphasized that the mass shift mentioned here represents net movement in axial projection. If cross-bridge I, say, moves upon activation, and concomitantly cross-bridge II moves into the location vacated by I, then the *net* mass movement associated with that location is zero despite the occurrence of major rearrangement. Therefore, the actual fraction of the total S-1 involved in the mass shift is likely to be substantially greater than these percentages suggest.

Consequences of Limited Resolution and Uncertainties in Intensity Measurements

In the difference map B_a - B_r (Fig. 5), the peak gain in mass is at the trigonal points, as if the attachment of cross-bridges produces a density increase at the centers of thin filaments. To examine this effect further, model calculations were made. They showed that if the thin filament were represented by a cylinder of uniform density and 7 nm diam, and if the diameter were increased to 11 nm with the same density, then at 12-nm resolution the peak gain in density indeed appeared to occur at the center. If the area was enlarged from 7 to 15 nm, then the feature of greatest gain appeared as an annular ring. This suggests that in transition from B_r to B_a, the net increase of mass around the thin filament is confined to a small area, 3–4 nm deep, immediately surrounding the actin filaments.

To clarify the question of whether the annular shell visualized surrounding the thick-filament backbone could be an artifact due to the cutoff at $(12 \text{ nm})^{-1}$ in the Fourier transforms, model calculations were performed (see Methods). Thick and thin filaments were represented by disks of appropriate sizes, and then band-limited at this resolution. The results showed that a small amount of sixfold symmetric interstitial mass was generated by this procedure, but its magnitude was far lower than that of the corresponding effects in the models considered here.

The average intensities of the higher orders in the active patterns have standard errors of the order of 10–30% of the mean values (Table I). Calculations were performed to test how the difference maps are affected if individual active intensities are increased or decreased by two standard errors of the mean (2 SEM) while the map of the relaxed state was kept constant (model B_r). The difference maps, so modified, all showed similar patterns of mass gain at the thin-filament sites and mass loss around the thick-filament backbone. The apparent sixfold symmetry of the deep loss regions was also essentially unchanged, except that if I_{30} was raised by 2 SEM in B_a, this sixfoldedness became less pronounced.

Disorder within the Lattice Derived from the Systematic Broadening of Reflection Peak Widths

The active pattern has broader reflection peaks than the relaxed pattern, especially for the higher orders. To obtain consistent results and acceptably good fits in curve-fitting, we found it necessary to constrain the width parameters of the peaks. The constraints can be explained in terms of various kinds of lattice disorder.

It has long been known (e.g., 31, 32) that the widths of diffraction peaks reflect the degree of crystallinity of the structure that gives rise to the diffraction patterns. For an infinite perfectly ordered crystal, the reflection peaks are delta functions. As different types of disorder affect the lattice or as the size of the crystal is decreased, the peak widths are broadened. The broadening in many cases varies systematically with reflection angle θ, depending on the type of disorder. For the relaxed sartorius, we found that the equatorial pattern with five orders can be adequately described with peak widths that vary linearly as a function of the reflection angle (see Appendix). This result suggests two points concerning the origin of the reflections. First, the linear increase in width is probably caused by a distribution in lattice spacings. On the average, the standard deviation of this distribution is ~3% of d_{10}. Second, broadening of the peaks due to submicroscopic crystal size is insignificant; otherwise Eq. 3 (Appendix) would contain a term that is independent of the reflection angle (31). This places a lower limit on the coherence length (size of the crystalline domain) of at least 650 nm, indicating that the lattice in a resting muscle is crystalline in regions comparable in size to the myofibril.

In the active state, an additional type of disorder is present in the lattice, since the least-squares fit becomes very poor if one does not include the term σ^s (in Eq. 3 of the Appendix), which is proportional to the square of the reflection angle. The requirement for this extra term indicates that a liquidlike disorder is an important factor in the activated muscle (32, 33). The equilibrium positions of neighboring unit cells are no longer rigidly defined, but are only described by a probability distribution of nearest-neighbor spacings. With the present data, we cannot be more specific about the origin of this disorder, although it may be caused, for example, by the asynchronous movement and random attachment of the cross-bridges, and/or

by transient random displacement of filament segments away from the equilibrium positions.

CONCLUSION

The present analysis resolves the axially projected thick filament of relaxed frog muscle into a backbone and an annular shell that surrounds the backbone and is separated from it by a region of lower density. The shell contains tilted or slewed S-1 moieties of myosin, while the backbone contains the LMM and the S-2. Upon activation, mass moves out of the shell toward the thin filament while the backbone region remains essentially unchanged. This observation provides evidence that physiological force generation involves azimuthal and radial motion of S-1, and that the backbone of the thick filament serves as a mechanically stable support matrix for the S-1 moieties.

APPENDIX

Procedure for Analyzing the Diffraction Patterns

Equatorial x-ray diffraction patterns from intact frog sartorius muscle show at least five distinct reflections. The innermost reflections *10* and *11* are strong and sharp. In the relaxed state the higher orders are relatively weak, but they are well defined and their widths appear to increase toward higher orders. In the active state, the higher-order peaks are substantially broader, so that they merge into each other and are barely above background (Fig. 1). To systematically extract intensity data from these patterns, a nonlinear least-squares curve-fitting routine was applied using a procedure based on the Marquardt-Levenberg method (12). The systematic broadening of the peak widths led us to conclude that the major underlying cause of broadening of the peaks in the relaxed state is due to a distribution of lattice spacing among the myofibrils. In the active state, an additional liquid-like type of disorder (32, 33) is introduced.

We assumed that each peak (i.e., the transmitted direct beam, *10*, Z-line reflection [8], *11, 20, 21, 30* on both sides of the center) is of Gaussian form

$$\frac{A_{hk}}{\sqrt{2\pi}\,\sigma_{hk}} \cdot \exp\left[-\frac{(X-X_{hk})^2}{2\,\sigma_{hk}^2}\right], \tag{A1}$$

and that the centers follow the indexing relation $X_{hk} = (h^2 + k^2 + hk)^{1/2} X_{10}$; the spacing of the Z-line was taken to be 0.7 d_{10}. Three parameters, A_{hk}, X_{hk}, and σ_{hk}, are required to describe each peak, where A_{hk} is the integrated intensity of the peak *hk* above background, X_{hk} is the position of the center of the peak, and σ_{hk} is the width of the peak. We assumed the counting statistics to follow the Poisson distribution. Accordingly, in performing the least-squares fit each term in the sum of squares of deviations was weighted by $1/y_i$, where y_i is the number of counts in channel *i*.

The background was assumed to be a function of the form

$$a_1 + a_2x + a_3x^2 + a_4 \exp(-a_5x). \tag{A2}$$

The exponential term was included to describe the scattering near the edges of the backstop.

During the initial stage of data fitting, the peak widths σ_{hk} were all treated as independent parameters, of which six were required for each half of a pattern. However, without any constraints, the widths for the weak reflections varied widely among different experiments. It was later found that the peak widths (except for the Z-reflection) can be fitted

TABLE III

STANDARD DEVIATIONS OF LATTICE SPACING DISTRIBUTIONS AMONG CRYSTALLINE DOMAINS $\Delta d_{10}/d_{10}$ AND OF INTER-UNIT CELL DISTANCES $\Delta X/d_{10}$

Experiment	State	$\bar{d}_{10}$	$(\Delta d_{10}/d_{10})$	$(\Delta X/d_{10})$
		Å		
2125	Relaxed	380	3.8%	~0
2133	Active	380	3.8%	7.3%
2147	Relaxed	373	1.4%	~0
2145	Active	380	2.0%	7.5%
2039	Relaxed	366	2.5%	3.0%
2041	Active	380	4.8%	6.7%
2087	Relaxed	373	5.1%	~0
2081	Active	360	4.8%	7.5%

satisfactorily with the following expression

$$\sigma_{hk}^2 = \sigma_c^2 + (\sigma_{hk}^d)^2 + (\sigma_{hk}^s)^2, \tag{A3}$$

where σ_c is the width of the direct beam and σ_{hk}^d is the line width due to the distribution of interfilament spacings.

$$\sigma_{hk}^d = \frac{\Delta d_{10}}{d_{10}}\theta_{hk}, \tag{A4}$$

where d_{10} is the average value of lattice spacing of *10*, Δd_{10} is the deviation from the mean value d_{10}, and θ_{hk} is the $(h^2 + k^2 + hk)^{1/2}$. Furthermore,

$$\sigma_{hk}^s = \frac{1}{d_{10}}\pi^2\left(\frac{\Delta X}{d_{10}}\right)^2\theta_{hk}^2, \tag{A5}$$

where σ_{hk}^s is the line width due to liquid-like disorder, i.e., "disorder of the second kind" (32, p. 227), and ΔX is the standard deviation in the distribution of distances between nearest-neighbor unit cells. It follows that σ_{hk}^d increases linearly and σ_{hk}^s increases quadratically with reflection angle θ_{hk}. Both terms σ^d and σ^s were always included in the fits. By applying indexing relations, the widths of all five peaks were described by only two independent parameters, which we chose to be σ_{10} and σ_{10}^d.

The results for σ_{10} and its components are shown in Table III. The widths for the higher orders can be easily derived from the indexing relation for θ_{hk}. The results show that in the relaxed state, the line widths are dominated by σ^d, while in full activation, σ^s becomes significant.

REFERENCES

1. Huxley, H. E. 1968. Structural difference between resting and rigor muscle; evidence from intensity changes in the low-angle equatorial x-ray diagram. *J. Mol. Biol.* 37:507–520.
2. Haselgrove, J. C., and H. E. Huxley. 1973. X-ray evidence for radial crossbridge movement and for the sliding filament model in actively contracting skeletal muscle. *J. Mol. Biol.* 77:549–568.
3. Lymn, R. W., and G. H. Cohen. 1975. Equatorial x-ray reflections and cross arm movement in skeletal muscle. *Nature (Lond.).* 258:770–772.
4. Haselgrove, J. C., M. Stewart, and H. E. Huxley. 1976. Crossbridge movement during muscle contraction. *Nature (Lond.).* 261:606–608.
5. Yu, L. C., J. E. Hartt, and R. J. Podolsky. 1979. Equatorial x-ray intensities and isometric force levels in frog sartorius muscle. *J. Mol. Biol.* 132:53–67.
6. Huxley, H. E., and W. Brown. 1967. The low-angle x-ray diagram of vertebrate striated muscle and its behavior during contraction and rigor. *J. Mol. Biol.* 30:383–434.
7. Elliott, G. F., J. Lowy, and B. M. Millman. 1967. Low-angle x-ray diffraction studies of living striated muscle during contraction. *J. Mol. Biol.* 25:31–45.
8. Yu, L. C., R. W. Lymn, and R. J. Podolsky. 1977. Characterization of a nonindexible equatorial x-ray reflection from frog sartorius muscle. *J. Mol. Biol.* 115:455–464.
9. Webb, N., S. Samson, R. Stroud, R. Gamble, and J. D. Baldeschweiler. 1976. Remotely controlled mirror of variable geometry for small angle diffraction with synchrotron radiation. *J. Appl. Cryst.* 10:104–110.
10. Gamble, R., J. D. Baldeschweiler, and J. Giffin. 1979. Linear position sensitive detector incorporating a self-scanning photodiode array. *Rev. Sci. Instrum.* 50:1416–1420.
11. Podolsky, R. J., R. St. Onge, L. C. Yu, and R. W. Lymn. 1976. X-ray diffraction of actively shortening muscle. *Proc. Natl. Acad. Sci. USA.* 73:813–817.
12. Knott, G. 1979. MLAB: a mathematical modeling tool. *Comput. Programs Biomed.* 10:271–280.
13. Trus, B. L., and A. C. Steven. 1981. Digital image processing of electron micrographs: the PIC system. *Ultramicroscopy.* 6:383–386.
14. Smith, P. R., and U. Aebi. 1976. The computer filtration of hexagonal lattices. *J. Supramol. Struct.* 5:493–495.
15. Squire, J. 1972. General model of myosin filament structure. *J. Mol. Biol.* 72:125–138.
16. Maw, M. C., and A. J. Rowe. 1980. Fraying of A-filaments into three subfilaments. *Nature (Lond.).* 286:412–414.
17. Ip, W., and J. Heuser. 1983. Direct visualization of the myosin cross-bridge helices on relaxed rabbit psoas thick filaments. *J. Mol. Biol.* 171:105–109.
18. Kensler, R. W., and M. Stewart. 1983. Frog skeletal muscle thick filaments are three-stranded. *J. Cell Biol.* 96:1797–1802.
19. Squire, J. 1974. Symmetry and three-dimensional arrangement of filaments in vertebrate striated muscle. *J. Mol. Biol.* 90:153–160.
20. Squire, J. 1981. The Structural Basis of Muscular Contraction. Plenum Publishing Corp., New York.
21. Hanson, J., and J. Lowy. 1963. The structure of F-actin and of actin filaments isolated from muscle. *J. Mol. Biol.* 6:46–60.
22. Barany, M., K. Barany, T. Rechard, and A. Volpe. 1965. Myosin of fast and slow muscles of the rabbit. *Arch. Biochem. Biophys.* 109:185–191.
23. Yates, L. D., and M. L. Greaser. 1983. Quantitative distribution of myosin and actin in rabbit skeletal muscle. *J. Mol. Biol.* 168:123–142.
24. Bragg, W. L., and M. F. Perutz. 1952. The structure of haemoglobin. *Proc. R. Soc. Lond. Ser. A Math. Phys. Sci.* 213:425–435.
25. McLachlan, A. D., and J. Karn. 1982. Periodic charge distributions in the myosin rod amino acid sequence match cross-bridge spacings in muscle. *Nature (Lond.).* 299:226–231.
26. Podolsky, R. J., G. R. S. Naylor, and T. Arata. 1982. Crossbridge properties in the rigor state. *In* Basic Biology of Muscles: A Comparative Approach. B. M. Twarog, R. J. C. Levine, and M. M. Dewey, editors. Raven Press, New York. 79–89.
27. Heuser, J. E. 1983. Structure of the myosin crossbridge lattice in insect flight muscle. *J. Mol. Biol.* 169:123–154.
28. Mendelson, R., and K. M. Kretzschmar. 1980. Structure of myosin subfragment from low-angle x-ray scattering. *Biochemistry.* 19:4103–4108.
29. Haselgrove, J. C. 1980. A model of myosin crossbridge structure consistent with the low-angle x-ray diffraction pattern of vertebrate muscle. *J. Muscle Res. Cell Motil.* 1:177–191.
30. Harrington, W. F. 1979. On the origin of the contractile force in skeletal muscle. *Proc. Natl. Acad. Sci. USA.* 76:5066–5070.
31. Guinier, A. 1963. X-ray Diffraction in Crystals, Imperfect Crystals, and Amorphous Bodies. W. H. Freeman & Co., New York.
32. Vainshtein, B. K. 1966. Diffraction of X-rays by Chain Molecules. Elsevier Publishing Co., Amsterdam.
33. Schwartz S., J. E. Cain, E. A. Dratz, and J. K. Blasie. 1975. An analysis of lamellar x-ray diffraction from disordered membrane multi-layer with application to data from retinal rod outer segments. *Biophys. J.* 15:1201–1230.
34. Egelman, E. H., and R. Padron. 1984. X-ray diffraction evidence that actin is a 100 Å filament. *Nature (Lond.).* 337:56–57.